A three-dimensional geometric quantification of human cortical canals using an innovative method with micro-computed tomographic data

Xavier Roothaer, Rémi Delille, Hervé Morvan, Bruno Bennani, Eric Markiewicz, Christian Fontaine

Micron 114 (2018) 62–71

A three-dimensional geometric quantification of human cortical canals using an innovative method with micro-computed tomographic data

X. Roothaer[a,*], R. Delille[a], H. Morvan[a], B. Bennani[a], E. Markiewicz[a], C. Fontaine[b]

[a] Univ. Valenciennes, CNRS, UMR 8201, LAMIH, F-59313 Valenciennes, France
[b] Department of Anatomy, Faculty of Medicine, University of Lille 2, Place de Verdun, 59045 Lille cedex, France

Keywords:
Cortical porosity
Canal orientation
Canal geometry
Canal connectivity

ABSTRACT

The complex architecture of bone has been investigated for several decades. Some pioneer works proved an existing link between microstructure and external mechanical loading applied on bone. Due to sinuous network of canals and limitations of experimental acquisition technique, there has been little quantitative analysis of three-dimensional description of cortical network. The aim of this study is to provide an algorithmic process, using Python 3.5, in order to identify 3D geometrical characteristics of voids considered as canals. This script is based on micro-computed tomographic slices of two bone samples harvested from the humerus and femur of male cadaveric subject. Slice images are obtained from 2.94 µm isotropic resolution. This study provides a generic method of image processing which considers beam hardening artefact so as to avoid heuristic choice of global threshold value. The novelty of this work is the quantification of numerous three-dimensional canals features, such as orientation or canal length, but also connectivity features, such as opening angle, and the accurate definition of canals as voids which ranges from connectivity to possibly another intersection. The script was applied to one humeral and one femoral samples in order to analyse the difference in architecture between bearing and non-bearing cortical bones. This preliminary study reveals that the femoral specimen is more porous than the humeral one whereas the canal network is denser and more connected.

1. Introduction

Cortical bone is the part of skeleton which provides mechanical properties and ensures resistance of bone to fracture. The macroscopic strength is strongly influenced by the micro-scale matrix which reveals a heterogeneous medium (Mirzaali et al., 2016; Bala et al., 2016). A 2D transverse slice of bone shows that tissue is composed of pores, called Haversian canals, enclosed by a lacuno-canalicular network called active osteonal bone (Buenzli and Sims, 2015; Ashique et al., 2017). This phase can be considered (in the transverse plane) as a circular shape surrounded by a thin wall (1–5 µm) called cement line. Pioneer work of Frost (1969) shows a correlation between cortical architecture and mechanical loading highlighting a remodelling activity named “Bone Multicellular Unit” (BMU) activity. More recent studies (Cooper et al., 2007; Hunter and Agnew, 2016; Bala et al., 2016) associated microscopic structure with bone strength, age or gender. Bala et al. (2016) reported an innovative method to collect 13 young ex-vivo fibula samples (age: 13.2 ± 3.5) compared with 16 older ex-vivo fibula samples (age: 75.0 ± 12.9). This study shows a negative correlation between pore volume fraction and age for both groups. Moreover, a great structure difference was found between growing children and adults reflecting the significant impact of BMU activity throughout a life. Mullins et al. (2007) observed, from a numerical 3D REV (Representative Element Volume) model of cortical bone, that maximum stresses were found near the intersections of Volkmann's and Haversian canals. However, orientation and angle between connected canals don’t fit with qualitative experimental results (Cooper et al., 2003; Bousson et al., 2004). Cooper et al. (2016) concluded that since 2000s, micro-computed tomography became the standard technique for the assessment of cortical architecture. The low resolution scanning (< 10 µm) offers the possibility to easily quantify vascular canals of ex-vivo samples. However, so far, little research report 3D geometrical analysis of tomographic data. In one of the most recent studies, Pratt and Cooper (2017) provides a 3D analysis of orientation for vascular canals in vertebrates. Nevertheless, data are limited to orientation and little number of animal samples. The aim of the paper is to provide a process to quantify 3D geometrical features for vascular canals in cortical bone. This method begins by an image processing which takes into account beam hardening in micro-CT slices in order to use Otsu threshold method (Otsu, 1979). Hence, generic parameters can be used for several

* Corresponding author.
E-mail address: xavierroothaer@gmail.com (X. Roothaer).

DOI : 10.1016/j.micron.2018.07.006

samples and qualitative choice of threshold value is avoided. 14 geometrical features are computed for each canal. According to current knowledge, this study is the first one to provide the quantification of connectivity features. Opening angle, defined as the angle between two connected canals, can be useful as input of microscopic numerical models of cortical bone. These experimental results will improve the understanding of bone architecture and will be useful as input data for the Human virtual modeling. In Section 2, the script is step-by-step described. A validation script for canals and connectivity features is also detailed. In Section 3, the absolute error is quantified and two bone samples are analysed in order to study cortical bone architecture differences.

2. Materials and methods

2.1. Specimens and sample preparation

One humerus and one femur samples were extracted from a 72 years-old male cadaveric subject (1.75 m, 70 kg) provided by the body donation bank Anatomy Laboratory. Care was taken to reduce bone drying by using a body embalming procedure (methanol, distilled water, glycerine and phenol solution) two days maximum post-mortem. Particular attention was paid to the extraction method and especially the location of the extraction site in the diaphysis. Indeed, throughout this paper, samples are denominated according the international nomenclature and the anatomic description of the diaphyseal side. Hence, the two samples are named 501HAMP and 501FAMP2 because they were extracted from AnteroMedial Proximal side of the corresponding diaphysis, respectively. Surgical and precision saws were used to obtain 60 × 10 × 1 mm segmental specimens oriented along the longitudinal axis of the diaphysis. These specimens were designed for tensile test (Bry, 2015).

2.2. Micro-CT scanning

Both samples were scanned using SkyScan 1172 high resolution desktop micro-CT (80 kV, 100 µA, rotation step: 0.25 degrees) at 2.94 µm isotropic voxel size. All micro-CT slices images are reconstructed using Nrecon 1.7.04 software. Due to high resolution, only 3 mm were scanned. Five hours scan times per sample were necessary to obtain 1021 slices images along the longitudinal axis.

2.3. Algorithm

This part of the article describes the algorithm step by step in the same order as the processing. Fig. 1 illustrates the five main steps. First, the image processing and contours detection are detailed, especially the threshold method. Second, the 3D link detection and canal construction are explained. Third, connectivities are detected and each canal is split at each intersection. Finally, canals are smoothed in order to compute more realistic canal and connectivity features.

2.3.1. Python version

The algorithm was carried out using Python 3.5 with OpenCV 3.2 (Bradski and Kaehler, 2011) for image processing and contours detection. Statistical data were obtained using Scipy 0.19 (Jones et al., 2001), Numpy 1.13 (van der Walt et al., 2011) and Pandas 0.20.1 libraries and plotted via Matplotlib 2.0.0 (Hunter, 2007).

2.3.2. Image processing

The first step of the algorithm is to read the slice images using OpenCV library and convert them into greyscale images (Fig. 1). In order to minimise noise effects, an adaptive threshold method was developed coupled with several filters. A bilateral filter is first applied to the raw picture. This filter is based on a blur algorithm but has the advantage to preserve edges of an image (Durand and Dorsey, 2002). Because of brightness difference due to parallelipipedical shape of the sample (beam hardening artefacts), a global thresholding method can't be used. The customised threshold method is based on the Otsu threshold algorithm (Otsu, 1979). It consists in splitting each image along the brightness difference axis and independently processes and thresholds inner and outer portions (Fig. 2). The number of portions is a user-specified input parameter and has to be chosen according width dimension of the sample. A short sensitivity study has shown that 5 portions is a suitable value in most cases. Indeed, the brightness of each kind of portions can be adjusted using a global gamma correction (Eq. (1))

$$P_{x_{\text{corrected}}} = 255*\left(\frac{P_x}{255}\right)^{\left(\frac{1}{\gamma}\right)} \tag{1}$$

As shown in Figs. 2 and 3, it is essential to apply additional filters to the thresholded image. Actually, dummy pixels are still visible out of bone matrix and near pores. These dummy pixels are created from local brightness differences which affect the threshold result. To reduce noise, morphological filter followed by a hierarchical filter are applied. The first one consists in removing isolated pixels (Gonzalez and Woods, 2008) on the thresholded image by applying subsequently an erosion and a dilation. The second one is applied after edge detection and keeps only contours which the parent is the sample contour (Fig. 3). Actually, the OpenCV function used to detect contours returns several outputs. One of these outputs indexes the parent of every contour. Hence, every contour located inside a canal pore or outside of the bone sample can easily be identified and removed. Contours are sorted according their area value. Therefore, it is possible easily identify the sample contour from pore contours (Fig. 3). One advantage of the above-described process is that it avoids the use of a qualitative global threshold value and generic values can be set: five portions per image applied with 0.5 gamma correction on inner portions give the best results.

2.3.3. 3D link detection & canals construction

Previous studies have reported a 3D interpretation of the cortical porosity using the skeletonisation algorithm (Pratt and Cooper, 2017; Cooper et al., 2003). However, these results focus only on few geometric features (orientation or length). In this study, a new 3D interpretation is proposed. The next step of the algorithm is the 3D link detection step between consecutive images (Fig. 1). Indeed, from the detected contours, moments (Bradski and Kaehler, 2011) are computed in order to obtain the area value of the contours (M_{00} moment), and to obtain the contour centroid coordinates (Eq. (2)).

$$\begin{pmatrix} \text{ctd}_x \\ \text{ctd}_y \\ \text{ctd}_z \end{pmatrix} = \begin{pmatrix} \frac{M_{10}}{M_{00}} \\ \frac{M_{01}}{M_{00}} \\ -i \end{pmatrix} \tag{2}$$

Centroid coordinates are written ctd_x, ctd_y, and ctd_z for x, y and z axes, respectively. Eq (2) shows that ctd_x and ctd_y are computed from contour moments. z coordinate is induced by longitudinal scanning. Hence, from these data, the contour's equivalent diameter can be computed. So as to create a 3D link between inter-slice contours, condition specified by Eq. (3) should be reached.

$$\sqrt{\left(\text{ctd}_{i,j_{1x}} - \text{ctd}_{i+k,j_{2x}}\right)^2 + \left(\text{ctd}_{i,j_{1y}} - \text{ctd}_{i+k,j_{2y}}\right)^2} \leq \text{Dm}_{i,j_1} \tag{3}$$

In other words, this condition means that the projected distance between contour j_1 from the ith image and contour j_2 from the $(i + k)$th image (left term on Eq. (3)) must be less than the equivalent diameter computed from the upstream contour, Dm_{i,j_1}, to be considered as a 3D link (see Fig. 1 for schematic interpretation). k is a user-specified parameter which represents the number of images to compare until link detection. Isolated contours are not considered further. Due to high resolution scanning, only canals with over five segments are considered (to reduce residual noise and edge-effects).

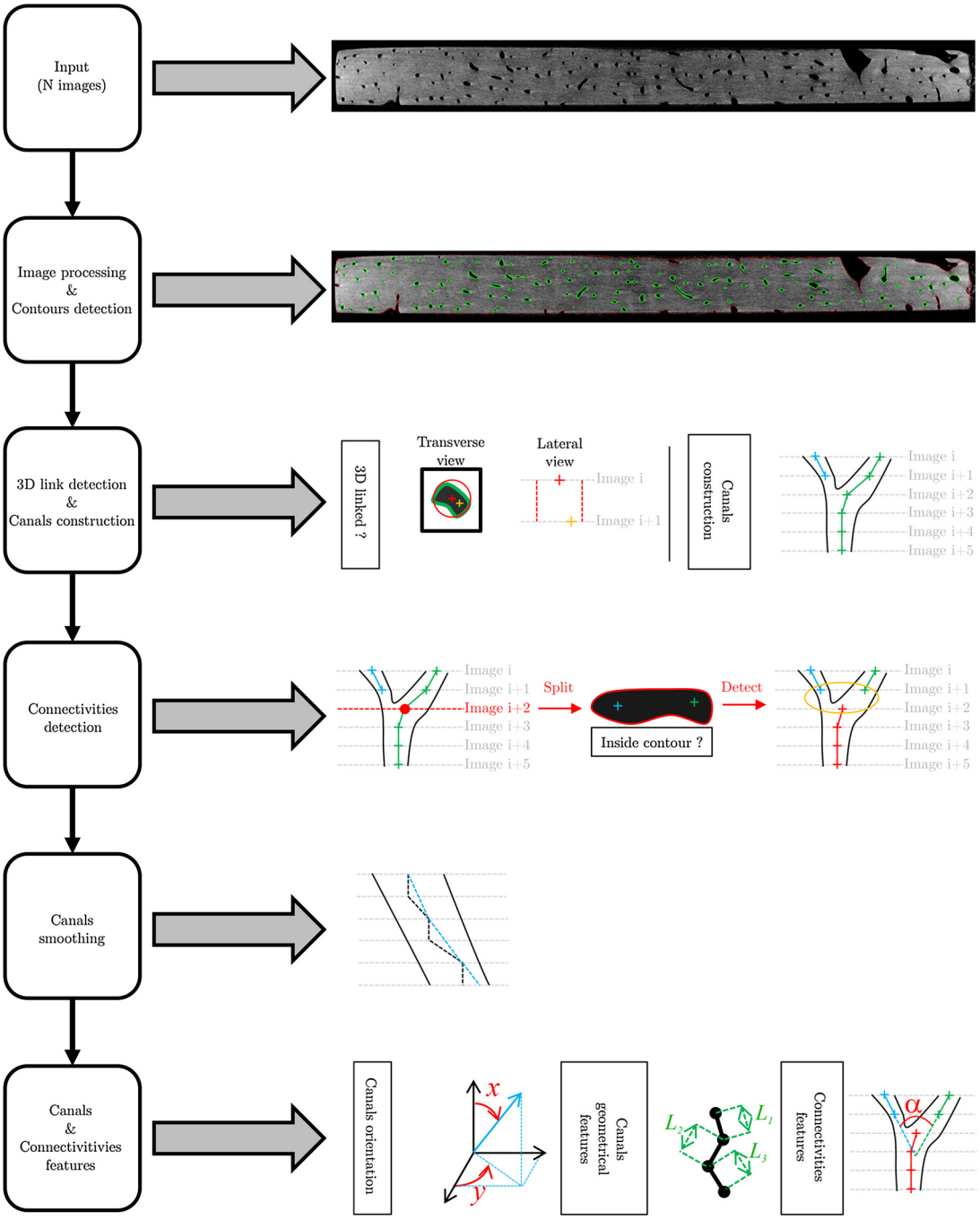

Fig. 1. Global overview of the algorithm.

3. D connectivity detection

Previous works done by Cooper et al. (2003) have shown that the cortical bone has a highly connected architecture. However, it is important to consider connectivity in order to obtain representative statistical values. Therefore, in this study, canals have to be split at each connectivity. At this stage in the proceeding, a set of canals is available (Fig. 4a). Nevertheless, these canals aren't necessarily split at each connectivity and can pass through several connectivity (see Fig. 1). Thus, an automated script is used to detect connectivity. Firstly, it consists in iterating each contour from each canal in order to detect the end of another canal inside the contour. If the end of a canal is inside the contour, the first canal is split at this point (Fig. 1). This first iteration splits all the canals at connectivities by detecting the end of another canal inside the contour. Then a second iteration performs the same test for each canal's end in order to detect connectivity.

2.3.4. 3D canals smoothing

In order to reduce the occurrence of jaggies on wire centroid line, canals are smoothed. Indeed, oriented canal can be perceived as a set of longitudinal segments with occasionally oriented segments (see Fig. 1, black wire line on Canals Smoothing scheme). To reduce this phenomenon, the algorithm detects the first point of every longitudinal segment so as to create a new wire line. This new wire line (Fig. 1, blue wire line on Canals Smoothing scheme) goes through on previously detected point. Other points are in-plane projected on the new wire line in order to keep z coordinate.

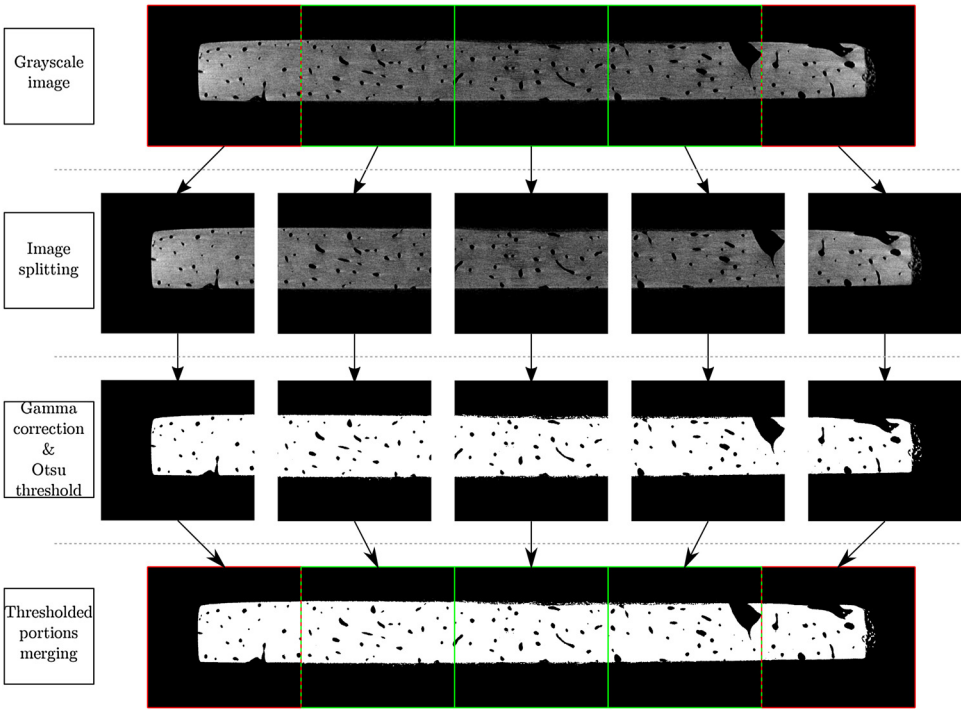

Fig. 2. Image thresholding step. This step follows the bilateral filter but precedes the morphological filter. The figure shows the example with five portions along the width of the sample with 0.5 gamma correction on inner portions (no gamma correction on outer portions). Inner and outer portions are green and red surrounded, respectively. This figure was generated from the raw image, without applying any filter so as to note threshold efficiency.

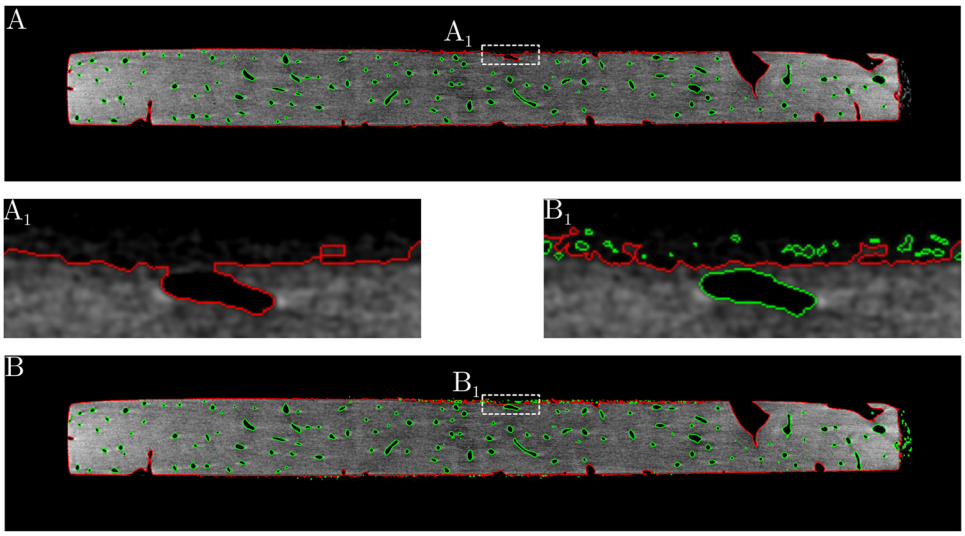

Fig. 3. Comparison between contours from the filtered image (Image A) and contours from the raw image (Image B). Same threshold parameters are set (5 portions with 0.5 gamma correction on inner portions). Sample contour is highlighted in red. Images A and B have 126 and 248 contours, respectively.

2.3.5. 3D canals and connectivities features

Thanks to numerous available data, considerable features can be computed. In order to standardise these features, a standard nomenclature (partially inspired by Parfitt (1988)) is employed. As a matter of fact, segment and canal features are preceded by Seg and Ca, respectively. According to the wire interpretation, each canal is considered as a set of segments which link two consecutive contours (see Fig. 4a and b). Hence, each feature is first computed from segments. Then, from segment features, canals characteristics are computed (Table 1).

Orientation. Orientation is derived in two stages. The first stage consists in considering 3D orientation using Euler angles. It comprises two consecutive rotations from the image plane (Fig. 4c). The first rotation, Theta (θ), represents the rotation about $\vec{y}$ axis. The second rotation, Psi (ψ), represents the rotation about $\vec{x'}$. In addition, considering cylindrical porosity, the normal of the red plane is collinear to the longitudinal axis of the cylinder (Fig. 4c). From this Euler angles, a second orientation system can be set (Fig. 4d). The main advantage of this orientation over the Euler's one is only one angle is useful to describe either the longitudinal orientation (angle x) or transverse orientation (angle y). Thereby, according to its mathematical formula (see Table 1), x ranges from 0 deg (longitudinal orientation) to 90 deg (transverse orientation). Likewise, y ranges from ± 90 deg (collinear with $\vec{y}$) to 0 deg (collinear with $\vec{x}$).

Length. Concerning length, two different features are computed: real and apparent length. The first one represents the centroid wire line length by summing all the segments length and the second one represents the height difference between segments ends for segment features (*Seg. aLe*) and distance between first and last point of canals for canal features (*Ca. aLe*). Segment apparent length is useful to compute segment volume whereas canal apparent length is used for canal 3D aspect ratio computing.

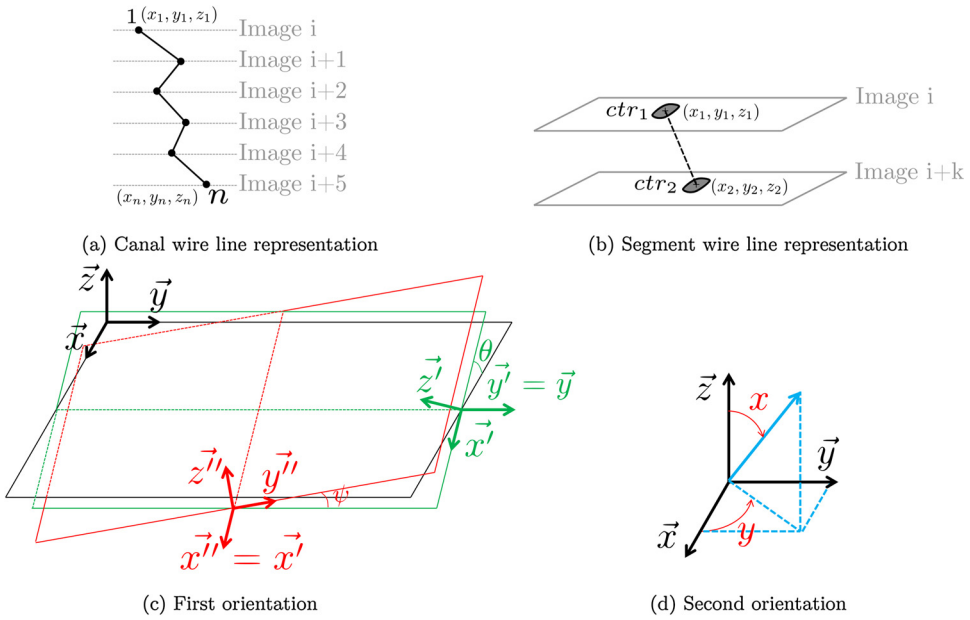

(a) Canal wire line representation

(b) Segment wire line representation

(c) First orientation

(d) Second orientation

Fig. 4. Canal interpretation. The canal wire line is a set of segments which link 2 inter-frame contours. (a) the canal wire-line connects each canal centroids indexed from 1 to n ($n-1$ segments). (b) This figure shows that each segment can link 2 contours (written ctr) spaced from k images. k is a user specified parameter (see Eq. (3) and explanations for more details). (c) The orientation is computed from Eulerian angles (θ and ψ). Black color is set for image plane. Green and red colors are set for intermediate plane and transverse plane of canal, respectively. Hence, the normal to the red plane represents the orientation of the canal. (d) A second orientation is computed from Eulerian angles (Table 1). This orientation is reduced to a longitudinal (x angle) and transverse orientation (y angle) relative to image plane coordinate system.

Surface and equivalent diameter. As specified above, surface value is obtained from contour moments using M_{00} moment. Therefore, equivalent diameter can be computed using Eq. (4). Segment features are obtained by averaging contour values (Fig. 4b and Table 1) and canal assessment is the average of segments characteristics.

$$\mathrm{Dm_{eq}} = \sqrt{\frac{4*M_{00}}{\pi}} \tag{4}$$

The novelty of this methodology is that it takes into account 3D orientation. Actually, assuming oriented cylindrical porosity, apparent surfaces perceived by slice images (elliptical shape) are larger than cylindrical transverse surfaces (circular shape). Consequently, directly computing equivalent diameter from slice images leads to biased results. Hence, apparent and real surfaces are related according Eq. (5).

$$\frac{\text{Real surface}}{\text{Apparent surface}} = \cos(x) \tag{5}$$

Volume and volume fraction. In order to obtain global volume fraction of the sample, usually called BV/TV, segment volume is computed from multiplication between apparent length and surface (Table 1). Then, each segment volume is summed to obtain canal volume. BV/TV is computed from the ratio between total canal volume and sample volume

$$\mathrm{BV/TV} = \frac{\sum_{i=1}^{N} \mathrm{Ca}_i.\ \mathrm{Vol}}{\text{Sample volume}} \tag{6}$$

2D & 3D aspect ratio. Two types of aspect ratio are computed for this purpose. 2D aspect ratio is obtained by dividing the width and length from bounding rotated rectangle of contour. In case of oriented cylindrical canals, 2D aspect ratio equals to $cos(x)$. Thus, it would be of

Table 1
Mathematical definition of canals features. Seg and Ca prefixes are related to Segment and Canal, respectively. All canal features are computed from segment features except for the apparent length and 3D aspect ratio which have either a different definition or aren't defined. Sample volume is obtained using the same formula for canal volume applied to contours of each slice which have the highest area value.

Features	Notation	Segment features	Canal features
ψ	ψ	Seg. $\psi = \tan^{-1}(\frac{y_2-y_1}{z_1-z_2})$	Ca. $\psi = \frac{1}{N}\sum_{i=0}^{N-1}$ Seg$_i$. ψ
θ	θ	Seg. $\theta = \tan^{-1}(\frac{x_1-x_2}{z_1-z_2})$	Ca. $\theta = \frac{1}{N}\sum_{i=0}^{N-1}$ Seg$_i$. θ
x	x	$Seg.\ x = cos^{-1}(cos(\psi) * cos(\theta))$	Ca. $x = \frac{1}{N}\sum_{i=0}^{N-1}$ Seg$_i$. x
y	y	Seg. $y = \tan^{-1}(\frac{-\sin(\psi)}{\cos(\psi)*\sin(\theta)})$	Ca. $y = \frac{1}{N}\sum_{i=0}^{N-1}$ Seg$_i$. y
Real Length	rLe	Seg. rLe $= \sqrt{(x_2-x_1)^2+(y_2-y_1)^2+(z_2-z_1)^2}$	Ca. rLe $= \sum_{0}^{N-1}$ Seg$_i$. rLe
Apparent length	aLe	$Seg.\ aLe = z_2 - z_1$	Ca. aLe $= \sqrt{(x_n-x_1)^2+(y_n-y_1)^2+(z_n-z_1)^2}$
Apparent surface	aS	Seg. aS $= \frac{\mathrm{ctr_1}.S+\mathrm{ctr_2}.S}{2}$	Ca. aS $= \frac{1}{N}\sum_{0}^{N-1}$ Seg$_i$. aS
Real Surface	rS	$Seg.\ rS = Seg.\ aS * cos(Seg.\ x)$	Ca. rS $= \frac{1}{N}\sum_{0}^{N-1}$ Seg$_i$. rS
Apparent Diameter	aDm	Seg. aDm $= \sqrt{\frac{4}{\pi}*\text{Seg. aS}}$	Ca. aDm $= \frac{1}{N}\sum_{0}^{N-1}$ Seg$_i$. aDm
Real Diameter	rDm	Seg. rDm $= \sqrt{\frac{4}{\pi}*\text{Seg. rS}}$	Ca. rDm $= \frac{1}{N}\sum_{0}^{N-1}$ Seg$_i$. rDm
Volume	Vol	$Seg.\ Vol = Seg.\ aL * Seg.\ aS$	Ca. Vol $= \sum_{0}^{N-1}$ Seg$_i$. Vol
Volume Fraction	$fVol$	Seg. fVol $= \frac{\mathrm{Seg.Vol}}{\mathrm{Sample.Vol}}$	Ca. fVol $= \sum_{0}^{N-1}$ Seg$_i$. fVol
2D aspect ratio	$AR2D$	Seg. AR2D $= \frac{1}{2}(\mathrm{ctr_1}.\ \mathrm{AR2}D + \mathrm{ctr_2}.\ \mathrm{AR2}D)$	Ca. AR2D $= \frac{1}{N}\sum_{0}^{N-1}$ Seg$_i$. AR2D
3D aspect ratio	$AR3D$	–	Ca. AR3D $= \frac{\mathrm{Ca.aLe}}{\mathrm{Ca.rDm}}$

Table 2
Mathematical definition of connectivity features. Conn prefix is used for each characteristic. $\overrightarrow{U_i}$ is obtained from the linear fitting of centroid wire line of the ith canal.

Features	Connectivity features
α	Conn. $\alpha = \lvert\cos^{-1}(\frac{\overrightarrow{U_1}\,.\,\overrightarrow{U_2}}{\lVert\overrightarrow{U_1}\rVert\,.\,\lVert\overrightarrow{U_2}\rVert})\rvert$
$R_{\mathrm{rDm}_{(0,12)}}$	Conn. $R_{\mathrm{rDm}_{(0,12)}} = \frac{\mathrm{Ca}_1\,.\,\mathrm{rDm} + \mathrm{Ca}_2\,.\,\mathrm{rDm}}{\mathrm{Ca}_0\,.\,\mathrm{rDm}}$
$R_{\mathrm{rDm}_{(1,2)}}$	Conn. $R_{\mathrm{rDm}_{(1,2)}} = \frac{\max(\mathrm{Ca}_1\,.\,\mathrm{rDm}, \mathrm{Ca}_2\,.\,\mathrm{rDm})}{\min(\mathrm{Ca}_1\,.\,\mathrm{rDm}, \mathrm{Ca}_2\,.\,\mathrm{rDm})}$

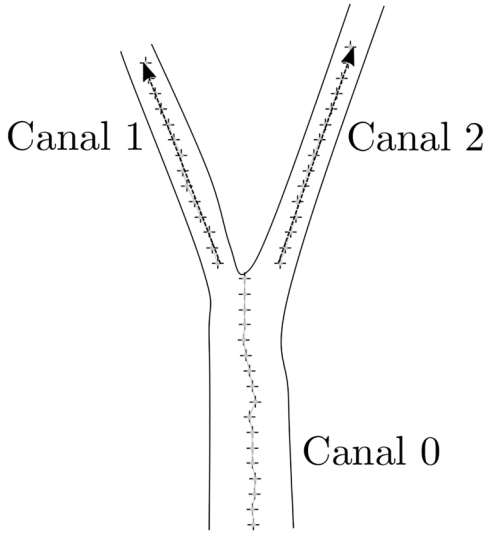

Fig. 5. Connectivity scheme. Arrows represent canals mean vectors $\overrightarrow{U_i}$.

interest to investigate this correlation between 2D and 3D features. 3D aspect ratio provides the general shape of the canal. Indeed, based on the straight cylindrical shape assumption for canals, this quantitative relation distinguishes flat shape porosity(< 1) from rod-like shape porosity(> 1).

Connectivity features. Connectivity detection provides possibilities for computing features. Actually, three geometric characteristics are carried out for canal intersections which links three canals at most (Table 2). The first feature, called opening angle, stands for the angle between linear fitting vector of outgoing canals (Fig. 5). The aim of this measure is to determine the statistical distribution in order to potentially link stress concentration with tight connectivity. Second and third features lend morphological information to intersections. $R_{\mathrm{rDm}_{(0,12)}}$ expresses the ratio between outgoing canals diameter sum and incoming canal diameter. If the ratio equals to 1, this means that the entire of the incoming canal diameter is split into 2 canals. Similarly, $R_{\mathrm{rDm}_{(1,2)}}$ expresses the diameter fraction between outgoing canals. If the ratio equals to 1, canals have the same diameter.

2.4. Algorithm validation

Due to original 3D interpretation of cortical porosity, an error estimating is required. For this purpose, a Python script was carried out by creating dummy slice images based on geometrical inputs using OpenCV library. Indeed, this algorithm assumes a parallelepipedic sample crossed by a user-specified number of oriented cylinder (Fig. 6). Orientation is specified by Euler angles. Cylinder diameter and position on the first slice image are indicated (Fig. 6b). The number of images depends on the resolution required by user and sample length. Ellipse position on the ith image is determined from Eq. (7).

$$\begin{cases} x_i = x_0 - i^{*}\tan(\theta) \\ y_i = y_0 + i^{*}\frac{\tan(\psi)}{\cos(\theta)} \end{cases} \tag{7}$$

3. Results and discussion

3.1. Script validation

In order to validate the algorithm processing, a set of images was generated. Sample length, width and thickness were 1.5, 10 and 2 mm, respectively. A 2.94 µm resolution was chosen to obtain 510 images. One cylindrical porosity with a diameter of 1.0 mm goes through the sample oriented along $\psi = 70$ deg and $\theta = 25$ deg Eulerian angles. Results are summed up in Table 3. This table is quite revealing in several ways. First, although the highly oriented canal, process is able to detect and predict its geometric features with an acceptable average error of 2.04%. Second, BV/TV can accurately be predicted from the

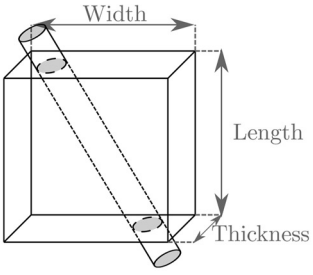

(a) Overview of sample dimensions

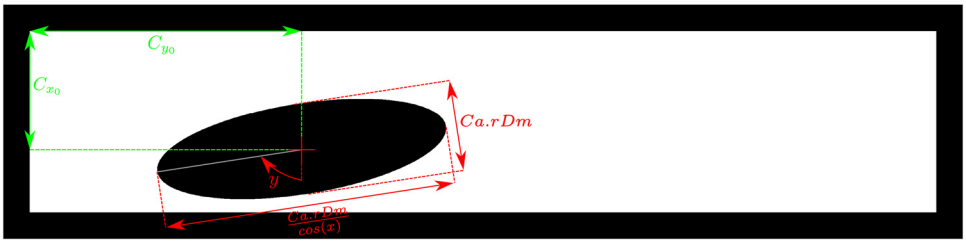

(b) First slice image

Fig. 6. Schematic representation of validation proceeding. The image on this figure was generated using the same input parameters as those used to obtain results outlined in Table 3.

Table 3
Comparison between theoretical and computing results.

Canal features	*Ca. ψ*	*Ca. θ*	*Ca. x*	*Ca. y*	*Ca. Vol*	*Ca. fVol*	*Ca. rLe*	*Ca. aLe*	*Ca. aS*	*Ca. rS*	*Ca. aDm*	*Ca. rDm*	*Ca. AR2D*	*Ca. AR3D*
	[deg]	[deg]	[deg]	[deg]	$[mm]^3$	[%]	[mm]	[mm]	$[mm]^2$	$[mm]^2$	[mm]	[mm]	–	–
Theoretical values	70.0	25.0	71.9	−81.3	3.8	12.6	4.8	4.8	2.5	0.8	1.8	1.0	0.3	4.8
Computational values	71.7	24.4	73.6	−82.3	3.8	12.7	4.8	4.8	2.5	0.7	1.8	0.96	0.3	5.0
Absolute error	2.47%	2.36%	2.29%	2.55%	1.06%	1.35%	0.09%	0.24%	0.51%	8.43%	0.26%	4.37%	0.73%	4.32%

Table 4
Descriptive statistics for canal features. BV/TV represents the cortical porosity computed from canal features. *Ca. D* is obtained from the total number of canals divided by the sample volume. Other characteristics are summed up using mean ± standard deviation.

Canals features		501FAMP2	501HAMP	Units
Volume porosity	*BV/TV*	7.55	4.73	%
Canal density	*Ca. D*	64.02	83.52	mm^{-3}
	Ca. x	28.77 ± 14.93	27.29 ± 14.56	deg
	Ca. y	−5.80 ± 41.71	5.69 ± 43.63	deg
	Ca. rDm	84.94 ± 60.93	62.35 ± 38.41	µm
	Ca. rLe	146.45 ± 180.62	186.79 ± 210.35	µm
	Ca. AR2D	0.57 ± 0.19	0.57 ± 0.20	–
	Ca. AR3D	2.39 ± 3.21	4.17 ± 5.50	–

canal volume fraction. Highest errors are obtained from the real surface, real diameter and 3D aspect ratio. These differences can be explained by the fact that these features accumulate inaccuracy from other characteristics. Indeed, for instance, real surface is obtained from the product of the apparent surface and $cos(x)$. Therefore, real surface cumulates errors of both features. One of the possibilities to reduce inaccuracy is to decrease scan resolution in order to have better edge description or to directly compute these features from raw image.

3.2. Canals features

As specified above, two specimens, obtained from same male subject, were analysed and compared. Mean values and standard deviation of canals features are summarised in Table 4. Likewise, histograms and box plots of canals features are shown in Fig. 8. Fig. 7 reflects the highly connected network of cortical vascular canals.

Table 4 provides the summary statistics for canal features. High values of standard-deviations indicate a wide statistic distribution of the canals features and the non-normal statistical distribution. This table reveals that the femoral sample is more porous than the humeral one. This difference could be explained by a different remodelling activity which is closely linked with the mechanical stimulus applied to the bone (Frost, 1969). In spite of the difference of porosity, humeral sample shows a denser canal network, with a diameter distribution which declines after a peak at [30, 40] µm (Fig. 8c). Concerning the femoral sample, the diameter distribution covers a broader band with 34.3% of canals with a diameter over 100 µm (15.6% for 501HAMP). Cooper et al. (2003) provide the distribution of canal diameters from 2 femoral samples where peaks were reached at [40-80] and [80, 160] µm, respectively. However, these results differ from some published studies (Bala et al., 2016; Bousson et al., 2004), where mean diameters are greater than those reported in the current study. Canals length distribution shows a similar behaviour for both sample (Fig. 8d). Indeed, most of canals range below a length of 200 µm. This value is fewer than the length reported by Cooper et al. (2003) study. However, a new canal definition is proposed and may differ from this previous study. Interestingly, length distribution suggests that canals with a length less than 100 µm should be considered (Pratt and Cooper, 2017; Farooq et al., 2017). Fig. 8e and f describes 2D and 3D aspect ratio, respectively. For both of these features, distribution is similar for humeral and femoral samples. *Ca. AR2D* distribution expresses that pore perceived by slice images should be rather considered as elliptic shape. Indeed, median and mean values about equal to 0.6 which means that the ratio between apparent and real surfaces equals to 0.6. This expresses that apparent surface is 40% overestimated and shows the importance of considering orientation for the surface and diameter computation. Interestingly, *Ca. AR3D* distribution shows a peak

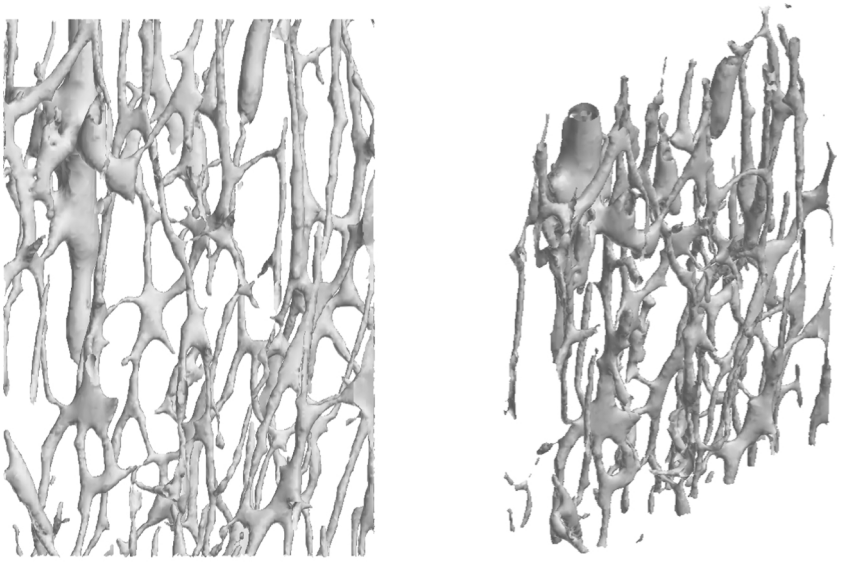

(a) Transverse view (b) Isometric view

Fig. 7. Three-dimensional rendering obtained from contours detection of 501HAMP sample. 3D surface reconstruction was obtained using Meshlab2016 (Cignoni et al., 2008). The volume is restricted to a subregion in order to make snapshot more visible.

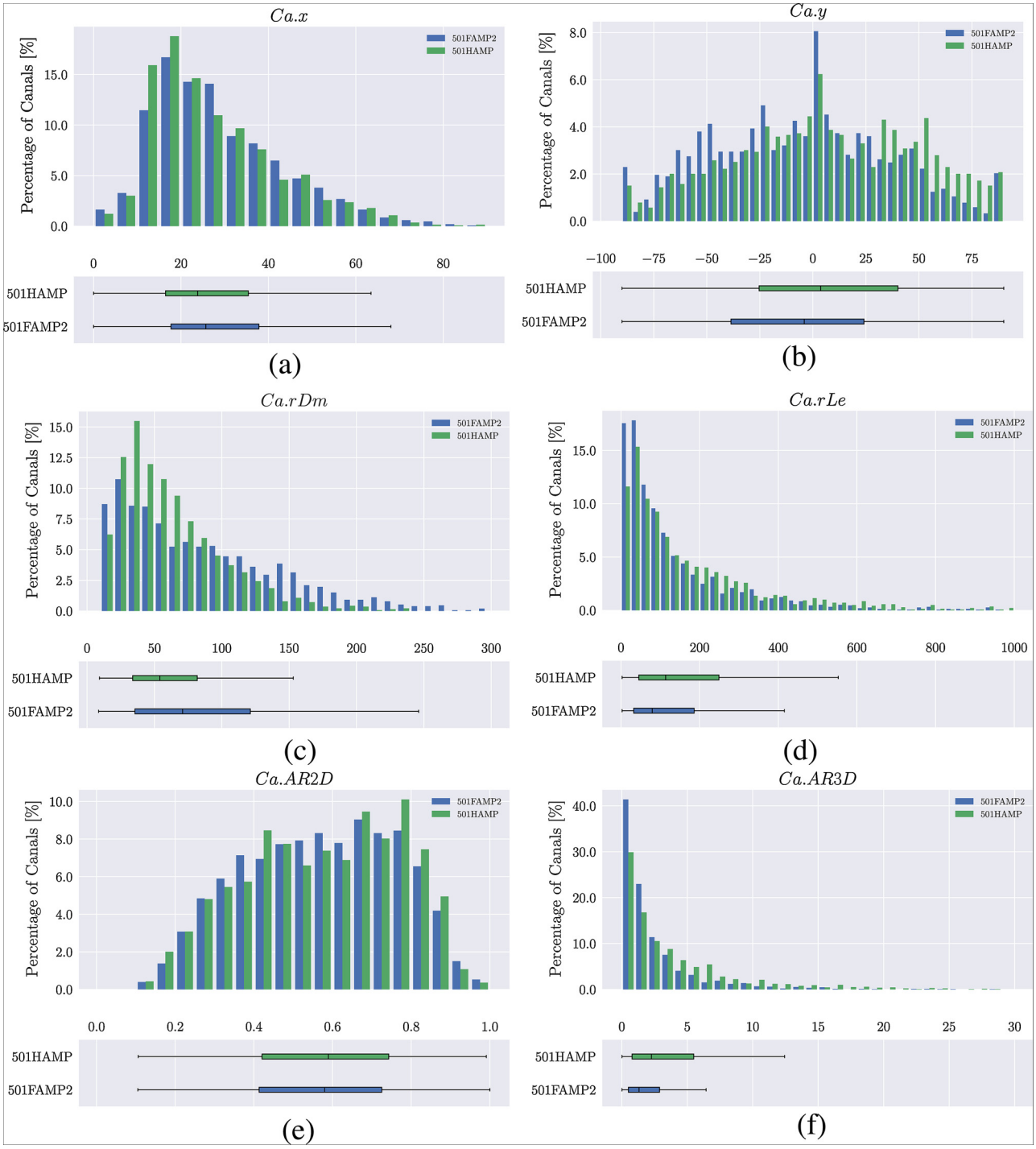

Fig. 8. Canals features histograms and box-plots of 501FAMP2 and 501HAMP are displayed in blue and green, respectively. Box-plots are horizontally plotted so as to share x-axis with the above histogram. Box-plots show min and max values (without outliers), 1st and 3rd quartiles with median value. Respective interval is indicated using [start, step, stop].

reached at [0, 1] interval. This means that, according to the new canal definition, most of canals have a flat three-dimensional shape. No experimental data was found to compare. Vandenbulcke et al. (2012) study reports a numerical sensitivity analysis of the void aspect ratio for the assessment of a multi-scale FE model. However, voids aspect ratio is much higher than computed experimental data. Fig. 8a and b shows distribution of longitudinal and transverse orientation, respectively. These figures are quite revealing in several ways. First, 3D link detection process is able to detect transverse canal (according Pratt and Cooper (2017) designation). Second, *Ca. x* distribution shows that global longitudinal orientation carries out along an oblique direction which isn't normal to transverse plane. This result fits with qualitative analysis of 3D scatter points obtained from contours detection in the image processing and with Bousson et al. (2004) study. Third, *Ca. y* distribution covers a broader band, which can be interpreted as a randomly arranged network in the transverse plane. Peak obtained at [0, 5] deg is explained by residual jaggies.

Table 5
Descriptive statistics for connectivity features. *Conn. D* is obtained from the total number of connectivities divided by the sample volume. Others characteristics are summed up using mean ± standard deviation

Connectivity features		501FAMP2	501HAMP	Units
Connectivitiy density	*Conn. D*	33.70	43.98	mm^{-3}
	Conn. α	38.00 ± 23.50	40.53 ± 21.46	deg
	Conn. $R_{\mathrm{rDm}_{(0,12)}}$	0.87 ± 0.37	0.85 ± 0.20	–
	Conn. $R_{\mathrm{rDm}_{(1,2)}}$	2.78 ± 2.34	1.99 ± 1.16	–

3.3. Connectivities features

Average ± standard deviation and statistical distribution of connectivity features are reported in Table 5 and Fig. 9, respectively.

Connectivity density is higher for the humeral sample than femoral one. This difference can be explained in part by the denser canal network in 501HAMP specimen. However, connectivity features have similar statistical distribution for both samples. Fig. 9a reveals that connectivities are essentially distributed between 30 and 50 degrees. Conn. $R_{\mathrm{rDm}_{(0,12)}}$ distribution (Fig. 9b) appears to be normal with a peak reached for [0.8, 0.9]. Likewise, Conn. $R_{\mathrm{rDm}_{(1,2)}}$ has a decreasing distribution (Fig. 9c) with a maximum attained for [1, 1.5] interval. Both these results suggest that canals are interconnected where most of outgoing canals (canals 1 and 2 in Figure 5) have same diameters. Furthermore, the sum of outgoing and incoming canal diameters have the same value. These results show that canals are interconnected with a privileged opening angle whatever the diameter. This conclusion is consistent with qualitative analysis found in several studies (Bousson et al., 2004; Cooper et al., 2003, 2007). This work leads to the conclusion that canals from same connectivity, have their diameter which can be closely linked with each other.

4. Conclusions

The purpose of the current study was to provide an original method to quantify 3D geometrical features for cortical porosity using micro-CT. This approach lends numerous canals features. This work is the first known study to quantify geometrical features for cortical connectivity. Thus, in order to obtain representative data, canals are defined as void which ranges from connectivity to possibly another one. The validation proceeding shows that this new method is able to compute accurate canals features. It also reveals that orientation has to be considered in order to don't overestimate the canal diameter. Experimental results suggest that cortical canals are oriented with an average angle of about 30 degrees relative to the longitudinal axis. Canals are randomly arranged in the transverse plane. The femoral sample is more porous with a broader canal diameter distribution whereas the humeral one has a

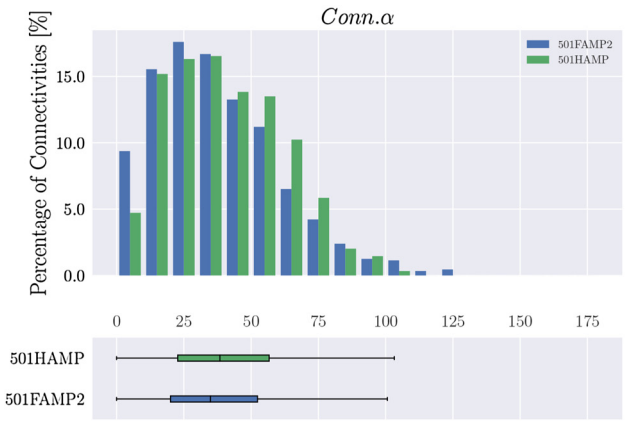

(a) $Conn.\alpha$ [0, 10, 180]

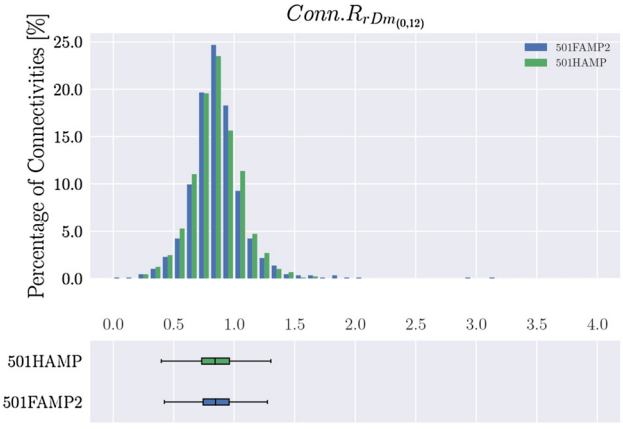

(b) $Conn.R_{rDm_{(0,12)}}$ [0, 0.1, 4]

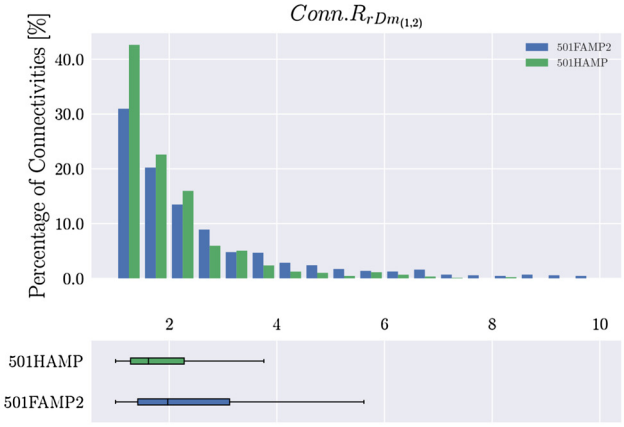

(c) $Conn.R_{rDm_{(1,2)}}$ [1, 0.5, 10]

Fig. 9. Connectivity features histograms and box-plots of 501FAMP2 and 501HAMP are displayed in blue and green, respectively. Box-plots are horizontally plotted so as to share the *x*-axis with the above histogram. Box-plots show min and max values (without outliers), 1st and 3rd quartiles with median value. Respective interval is indicated using [start, step, stop].

denser connected network. Connectivity features reveal similar statistical results for both specimens. However the current investigation was limited to two bone samples. It might be interesting to extend this study to more bone samples in order to make a more general conclusion and correlate results with age, gender or morphological parameters of human subjects. Moreover, connectivity opening angle distribution would be useful so as to investigate local stress concentration during a mechanical loading of bone matrix. This study brings encouraging results and could be extended to the quantification of bone remodelling by detecting BMU activity using geometrical criteria (Buenzli et al., 2011).

Acknowledgements

This research is funded by the French Ministry of Higher Education and Research and is carried out within the framework of the CNRS Research Federation on Ground Transports and Mobility, in articulation with the ELSAT2020 project supported by the European Community, the Hauts de France Regional Council. The authors gratefully acknowledge the support of these institutions.

References

Ashique, A.M., Hart, L.S., Thomas, C.D.L., Clement, J.G., Pivonka, P., Carter, Y., Mousseau, D.D., Cooper, D.M.L., 2017. Lacunar-canalicular network in femoral cortical bone is reduced in aged women and is predominantly due to a loss of canalicular porosity. Bone Reports 7 (Supplement C), 9–16.

Bala, Y., Lefevre, E., Roux, J.-P., Baron, C., Lasaygues, P., Pithioux, M., Kaftandjian, V., Follet, H., 2016. Pore network microarchitecture influences human cortical bone elasticity during growth and aging. J. Mech. Behav. Biomed. Mater. 63, 164–173.

Bousson, V., Peyrin, F., Bergot, C., Hausard, M., Sautet, A., Laredo, J.-D., 2004. Cortical bone in the human femoral neck: three-dimensional appearance and porosity using synchrotron radiation. J. Bone Miner. Res. 19 (5), 794–801.

Bradski, G.R., Kaehler, A., 2011. Learning OpenCV: computer vision with the OpenCV library, 1st ed. Software that sees., O'Reilly, Beijing oCLC:838472784.

Bry, R., 2015. Contribution l'etude de la variabilite des proprietes mecaniques de l'os cortical diaphysaire d'un os porteur (femur) et non-porteur (humerus). Valenciennes (Ph.D. thesis).

Buenzli, P.R., Sims, N.A., 2015. Quantifying the osteocyte network in the human skeleton. Bone 75 (Supplement C), 144–150.

Buenzli, P.R., Pivonka, P., Smith, D.W., 2011. Spatio-temporal structure of cell distribution in cortical Bone Multicellular Units: a mathematical model. Bone 48 (4), 918–926.

Cignoni, P., Callieri, M., Corsini, M., Dellepiane, M., Ganovelli, F., Ranzuglia, G., 2008. MeshLab: an Open-Source Mesh Processing Tool. In: Scarano, V., Chiara, R.D., Erra, U. (Eds.), Eurographics Italian Chapter Conference. The Eurographics Association.

Cooper, D., Turinsky, A., Sensen, C., Hallgrmsson, B., 2003. Quantitative 3d analysis of the canal network in cortical bone by micro-computed tomography. Anatom. Record Part B: New Anatom. 274B (1), 169–179.

Cooper, D.M.L., Thomas, C.D.L., Clement, J.G., Turinsky, A.L., Sensen, C.W., Hallgrmsson, B., 2007. Age-dependent change in the 3d structure of cortical porosity at the human femoral midshaft. Bone 40 (4), 957–965.

Cooper, D.M.L., Kawalilak, C.E., Harrison, K., Johnston, B.D., Johnston, J.D., 2016. Cortical bone porosity: what is it, why is it important, and how can we detect it? Curr. Osteopor. Reports 14 (5), 187–198.

Durand, F., Dorsey, J., 2002. Fast bilateral filtering for the display of high-dynamic-range images. Proceedings of the 29th Annual Conference on Computer Graphics and Interactive Techniques. SIGGRAPH '02. ACM, New York, NY, USA 257–266.

Farooq, S., Leussink, S., Sparrow, L.M., Marchini, M., Britz, H.M., Manske, S.L., Rolian, C., 2017. Cortical and trabecular morphology is altered in the limb bones of mice artificially selected for faster skeletal growth. Sci. Reports 7 (1).

Frost, H.M., 1969. Tetracycline-based histological analysis of bone remodeling. Calcif. Tissue Res. 3 (3), 211–237.

Gonzalez, R.C., Woods, R.E., 2008. Digital Image Processing, 3rd ed. Pearson/Prentice Hall, Upper Saddle River, NJ oCLC:255942782.

Hunter, R.L., Agnew, A.M., 2016. Intraskeletal variation in human cortical osteocyte lacunar density: implications for bone quality assessment. Bone Reports 5 (Supplement C), 252–261.

Hunter, J.D., 2007. Matplotlib: A 2d Graphics Environment. Comput. Sci. Eng. 9 (3), 90–95. http://ieeexplore.ieee.org/document/4160265/.

Jones, E., Oliphant, T., Peterson, P., et al., 2001. SciPy: Open source scientific tools for Python.

Mirzaali, M.J., Schwiedrzik, J.J., Thaiwichai, S., Best, J.P., Michler, J., Zysset, P.K., Wolfram, U., 2016. Mechanical properties of cortical bone and their relationships with age, gender, composition and microindentation properties in the elderly. Bone 93 (Supplement C), 196–211.

Mullins, L.P., McGarry, J.P., Bruzzi, M.S., McHugh, P.E., 2007. Micromechanical modelling of cortical bone. Comput. Methods Biomech. Biomed. Eng. 10 (3), 159–169.

Otsu, N., 1979. A threshold selection method from gray-level histograms. IEEE Trans. Syst. Man Cybern. 9 (1), 62–66.

Parfitt, A., 1988. Bone histomorphometry: Standardization of nomenclature, symbols and units (summary of proposed system). Bone 9 (1), 67–69.

Pratt, I.V., Cooper, D.M.L., 2017. A method for measuring the three-dimensional orientation of cortical canals with implications for comparative analysis of bone microstructure in vertebrates. Micron 92, 32–38.

van der Walt, S., Colbert, S.C., Varoquaux, G., 2011. The NumPy array: a structure for efficient numerical computation. Comput. Sci. Eng. 13 (2), 22–30. http://ieeexplore.ieee.org/document/5725236/.

Vandenbulcke, F., Rahmoun, J., Morvan, H., Naceur, H., Drazetic, P., Fontaine, C., Bry, R., 2012. On the mechanical characterization of human humerus using multi-scale continuum finite element model. 2012 IRCOBI conference, Dublin 598–610.